

# Validation of a low-dissipation Finite-Volume solver for implicit Large-Eddy Simulation

Giove De Cosmo<sup>a,\*</sup>, Luca di Mare<sup>a</sup>, Mauro Carnevale<sup>b</sup>

<sup>a</sup> Oxford Thermofluids Institute, University of Oxford, Oxford, OX2 0ES, United Kingdom

<sup>b</sup> Dipartimento di Ingegneria e Scienze Applicate, University of Bergamo, Bergamo, 24044, Italy

## ARTICLE INFO

### Keywords:

CFD  
Finite-volume method  
Turbulence modelling  
Implicit large-eddy simulation  
Numerical dissipation  
Wall-bounded flows

## ABSTRACT

In the field of turbulent flow modelling, implicit Large-Eddy Simulation (ILES) is appealing for its low cost and ease of implementation. Such advantages rely on the absence of a sub-grid scale model, since the dissipation of the numerical scheme is assumed to match the behaviour of unresolved turbulence. The implementation of an ILES model in traditional Unsteady-RANS codes for Computational Fluid Dynamics is not a straightforward exercise, as most of the classical schemes used for the discretisation of the Navier–Stokes equations prove too dissipative. This work presents a low-dissipation fix for the traditional Flux-Difference Splitting scheme of Roe in the context of Finite-Volume discretisations. The fix consists in selectively scaling the eigenvalues of the Roe matrix to lower the numerical dissipation as needed, by means of a scalar parameter. The low-dissipation version of the Roe scheme is implemented in an existing Finite-Volume compressible wall-resolved URANS code, to obtain an ILES model. The solver is first verified on a fundamental test case, i.e. vortex transport in uniform flow. The scalar parameter is then properly calibrated on the decay of Homogeneous Isotropic Turbulence, to ensure physical meaningfulness. A robust validation of the ILES model is finally presented on realistic turbulent flows. Results show that a relatively simple fix can achieve excellent agreement with the benchmark DNS data on a flat-wall channel flow and a bumped-wall channel flow.

## 1. Introduction

Large-Eddy Simulation (LES) is a high-fidelity turbulence resolving approach, where the turbulent energy cascade is modelled only for the smallest (sub-grid) scales, whereas the majority of the turbulent spectrum (usually more than 70%) is resolved [1]. This requires the use of fine grids and small timesteps, in order to achieve a sufficient spatial and temporal resolution. The advantage of LES over higher-fidelity approaches, as Direct-Numerical Simulation (DNS), clearly resides in its lower cost and suitability for industrial applications.

The mathematical basis of LES is the system of Favre (spatial) filtered Navier–Stokes equations. The Favre decomposition is defined as  $f = \bar{f} + f''$  and the Favre-filtered variable as  $\bar{f}(\bar{x}, t) = \frac{\rho \bar{f}}{\bar{\rho}}$ , where the bar ( $\bar{f}$ ) indicates filtering and  $\rho$  is the fluid density. The Favre-Filtered Navier–Stokes equations (FFNS) read

$$\frac{\partial \bar{\rho}}{\partial t} + \frac{\partial}{\partial x_j} (\bar{\rho} \bar{u}_j) = 0 \quad (1)$$

$$\frac{\partial \bar{\rho} \bar{u}_i}{\partial t} + \frac{\partial}{\partial x_j} (\bar{\rho} \bar{u}_j \bar{u}_i) = -\frac{\partial \bar{p}}{\partial x_i} + \frac{\partial}{\partial x_j} (\bar{\tau}_{ij} + t_{ij}^{SF}) \quad (2)$$

$$\frac{\partial \bar{\rho} \bar{E}}{\partial t} + \frac{\partial}{\partial x_j} (\bar{u}_j (\bar{\rho} \bar{E} + \bar{p})) = -\frac{\partial \bar{q}_j}{\partial x_j} + \frac{\partial \bar{u}_i \bar{\tau}_{ij}}{\partial x_j} + (\text{additional terms}) \quad (3)$$

where  $u$  is velocity,  $p$  is pressure,  $E$  is the total energy per unit mass,  $\bar{\tau}_{ij}$  is the Favre-filtered laminar shear stress,  $t_{ij}^{SF}$  is the Favre-filtered sub-filter scale stress tensor and  $\bar{q}_j$  is the Favre-filtered heat flux. Further details about the additional terms in the energy equation can be found in [2,3]. The use of standard filtering on pressure and density ( $\bar{p}$  and  $\bar{\rho}$ ) and Favre filtering on all other quantities allows the equation of state and the continuity equation to be free from sub-filter contributions.

Similarly to the Reynolds-Averaged Navier–Stokes (RANS) equations, the FFNS equations contain terms computed on the Favre-filtered variables ( $\bar{\tau}_{ij}$ ) and terms that need to be modelled to achieve closure ( $t_{ij}^{SF}$ )

$$\bar{\tau}_{ij} = 2\mu \left[ \frac{\partial \bar{u}_i}{\partial x_j} + \frac{\partial \bar{u}_j}{\partial x_i} - \frac{2}{3} \frac{\partial \bar{u}_k}{\partial x_k} \delta_{ij} \right] \quad t_{ij}^{SF} = -\bar{\rho} (\overline{u_i u_j} - \bar{u}_i \bar{u}_j) \quad (4)$$

The Sub-Grid Scale (SGS) modelling in LES accounts for the contribution of the sub-filter scale stress tensor  $t_{ij}^{SF}$  and mimics the energy transfer from the resolved to the unresolved scales of turbulence [4]. It mainly has a dissipative nature and it is aimed at extracting energy from the flow. Generally, sub-grid scale models are much simpler than Reynolds-Averaged Navier–Stokes (RANS) turbulence models and rely

\* Corresponding author.

E-mail address: [giove.decosmo@eng.ox.ac.uk](mailto:giove.decosmo@eng.ox.ac.uk) (G. De Cosmo).

on fewer hypotheses, as they have to account for a reduced number of physical phenomena. From a turbulence modelling perspective, LES can hence be considered less-sophisticated than Unsteady-RANS, as it implies solving at most one (usually algebraic) equation for SGS modelling, rather than transport and diffusion of turbulent properties (e.g.  $k$ ,  $\epsilon$  or  $\omega$ ). On the other hand, achieving higher-fidelity requires solving the Navier–Stokes equations on finer discretisations and carefully handling the boundary conditions. Furthermore, numerical schemes for LES must guarantee that the numerical dissipation introduced by the spatial discretisation of the convective fluxes is much lower than the SGS contribution. Usually, this is strictly verified only by high-order numerical schemes, namely the ones based on finite-differences or finite-element methods.

Industrial applications of LES are slowly emerging and they mainly rely on the adaptation of existing URANS solvers to a new high-fidelity framework. Current codes are often based on unstructured Finite-Volume formulations built on classical spatial discretisation schemes (rarely higher than 2nd order) to simplify the design and ease the implementation. A variety of LES studies in the literature have shown that the SGS model terms have the same order of magnitude as the truncation errors of many numerical algorithms. The high-dissipative nature of such discretisations poses questions about the actual need for a dissipative SGS model and how it interacts with the numerical viscosity of the scheme.

A simplified approach to LES, namely implicit-LES or iLES, exploits the numerical dissipation embedded in the unlimited upwind scheme to model the dynamics of the sub-filter scales. Further details about the rationale behind iLES can be found in Grinstein et al. [5]. From a practical perspective, no SGS model is used in iLES and the sub-filter shear stress tensor is simply neglected. The high-fidelity computation hence reduces to a laminar simulation on a sufficiently fine grid, adopting a timestep small enough. The high refinement of the spatial and temporal discretisations is the only characteristic that distinguishes the iLES from a Very Large-Eddy Simulation (VLES) or from a laminar simulation.

A universal numerical method for iLES does not exist and generally, non-oscillatory methods for shock flows (i.e. shock-capturing methods) are preferred. In fact, the artificial viscosity injected in such schemes mimics the physical production of entropy across a shock-wave and hence represents a robust *physical* condition. The iLES (or MILES) approach was first suggested by Boris [6], and it was based on monotone convection algorithms, as they were deemed adequate to intrinsically satisfy the physical requirements for a SGS model. Boris [6] referenced the Flux-Corrected Transport (FCT) algorithms, but later recognised that a number of other monotone schemes suited the same requirements. Among these, Grinstein et al. [5] mention the Piecewise Parabolic Method (PPM) [7] and Total Variation Diminishing (TVD) algorithms [8,9].

Most of the 2nd order numerical methods commonly used for the computation of compressible flows in the context of Finite-Volume Method are too dissipative to be employed in iLES. Incompressible codes are generally better suited to high-fidelity applications, but the adaptation of a compressible solver to LES is advantageous in making the tool multi-purpose and capable of handling a wide variety of flow regimes. It has been formally proved that the numerical dissipation introduced by compressible flow schemes does not scale correctly for Mach numbers approaching zero, affecting accuracy [10]. This category includes the classical first-order and second-order upwind schemes.

Lower dissipation schemes have been specifically developed for iLES. Recent examples include the Simple Low-dissipation AUSM (SLAU) scheme [11], and various applications of the high-order Discontinuous Galerkin method, e.g. Uranga et al. [12]. Higher-order Finite-Volume schemes based on intra-cell reconstructions (as the k-exact method [13, 14]) could also be considered for iLES. However, in some cases the numerical dissipation can prove too low to correctly account for the effect of the sub-filter scales. The need to match the dissipation of the

scheme to the physical decay of turbulence makes the implementation of an implicit-LES module in traditional Unsteady-RANS Finite-Volume solvers non-trivial.

Despite its undesired side effects on turbulence modelling, a classical Godunov-type Finite-Volume scheme requires some numerical dissipation to resolve the cell-to-cell discontinuity and stabilise the calculation. This is conveniently achieved using upwind-type Riemann solvers (as Roe approximate Riemann solver) in conjunction with high-order intra-cell reconstructions, useful to reduce and control the dissipation. Camarri et al. [15] state that the effects of the numerical dissipation and the SGS model should be separated as much as possible. Therefore, they suggest the use of a dynamic Smagorinsky model in conjunction with an upwind parameter, used to lower the numerical dissipation of the scheme.

Building on the work of Camarri et al. [15], Amirante and Hills [16] propose the use of an unlimited version of the Monotonic Upstream-centred Scheme for Conservation Laws (MUSCL), built on a 2nd order reconstruction (based on Barth and Jespersen [17]) coupled to a low-dissipation version of Roe approximate Riemann solver. The latter is tuned with a scalar parameter  $\epsilon$ , to be set to the minimum value needed to stabilise the calculation. Setting  $\epsilon = 0$  is not possible, as it reduces the upwind scheme to a central discretisation, leading to unbounded oscillations. Results on a turbulent channel flow and on a turbulent stator–rotor annular cavity show that the iLES can lead to results comparable to those obtained with the Smagorinsky model.

The low-dissipation upwind schemes adapted to iLES often present a rather crude tuning of the numerical viscosity based on stability arguments, without considering the effects on the simulated turbulent decay. This paper proposes a versatile low-dissipation fix for Roe approximate Riemann Solver based on a bespoke scaling of the linear/non-linear eigenvalues of the scheme. The value of the scaling parameter is robustly calibrated on a fundamental turbulence test case, namely the decay of Homogeneous Isotropic Turbulence. A detailed validation of the low-dissipation setup is carried out on classical wall-bounded turbulent flows. Overall, this paper aims to present a robust framework for the porting of an industrial-oriented URANS code to LES.

## 2. Methodology

### 2.1. The solver Zephyrus

The in-house Computational Fluid Dynamics (CFD) solver Zephyrus is a C++ cell-centred Finite-Volume code that solves the unsteady Favre-Averaged Navier–Stokes equations on unstructured meshes. It has been built on the same data structure of the solver AU3X, documented by di Mare et al. [18], Hadade et al. [19] and Wang et al. [20]. Trustworthiness in solutions has been validated against benchmark test cases in Carnevale et al. [21]. The solver then has been exercised and validated for realistic turbomachinery applications, as in Carnevale et al. [22], Wang et al. [23,24]. In contrast to other open-source packages, Zephyrus has been explicitly conceived to deal with the simulation of turbomachinery flows [25].

The computational grid is based on simplicial elements and the topology is face-based. Hexahedral grids are used throughout this study. The flow variables are stored at the cell centres. The boundary conditions are imposed using a ghost-cell approach, where a conformal layer of grid cells is created outside the domain by mirroring the position of the cells adjacent to the boundary. The correct number of conditions to be set on each boundary is based on characteristic theory. Subsonic inflow boundaries require 4 values quantities to be specified: total pressure  $p^0$  (or mass-flow rate  $\dot{m}$ ), total temperature  $T^0$  and the velocity vector  $\hat{u} = [\hat{u}_x, \hat{u}_y, \hat{u}_z]$ . Subsonic outflow boundaries require only 1 value to be specified, i.e. static pressure  $p$ . The URANS solver allows for wall-modelling, but the version used for iLES is wall-resolved. This requires computational grids to be sufficiently refined close to the viscous walls.

Cell-centred flow gradients are computed using a Weighted-Least Square (WLSQ) procedure [26]. Fluxes are evaluated at the cell-to-cell interface. Inviscid fluxes are computed using Roe approximate Riemann solver. The Unstructured-MUSCL (U-MUSCL) scheme proposed by Nishikawa [27] is employed to achieve nominal second order spatial discretisation. The gradient-based reconstruction is limited face-wise using the Van Leer limiter, comparing the face left/right slope to the centre-to-centre slope. Viscous fluxes at the cell interfaces are computed on the distance-averaged solution and gradient at the cell centres straddling the face. Source terms are assumed piecewise constant in the cell.

Turbulence modelling in the solver is based on the Unsteady-RANS (URANS) approach. The Boussinesq assumption is adopted and the turbulent viscosity can be computed using a range of turbulence closures, including  $k-\omega$  [28] and  $k-\varepsilon$  [29]. However, URANS has not been used in this work. The working fluid is calorically perfect air, where  $\gamma = 1.4$  and the Prandtl number is  $Pr = 0.72$ . The dependence of viscosity on absolute temperature is evaluated with Sutherland's law.

Pseudo time-marching is used for steady solutions, based on a 1st order backward Euler implicit formulation. This is equivalent to a relaxed Newton's method for non-linear iterations. The solver is semi-implicit and matrix-free, as the Jacobian is not stored. The first approximation to the non-linear update is computed explicitly. The linear system is then solved by fixed-point iteration, using the Jacobi preconditioner (i.e. Jacobi method). The formulation of the linear residual only requires the projection of the Jacobian in the direction of the current approximation of the update. The Jacobi preconditioner, i.e. the diagonal of the flux Jacobian, is approximated by its spectral radius, accumulated across the cell interfaces. This avoids the calculation of the full Jacobian matrix. Time accurate solutions are obtained by dual time stepping, based on a 2nd order backward Euler scheme. Further details can be found in Blazek [30].

## 2.2. Low-dissipation setup

In the context of implicit-LES, a high-fidelity module could be derived from the existing solver simply discarding the turbulence closures (i.e. running a laminar simulation). However, as previously discussed, the amount of numerical dissipation introduced by Roe numerical flux is too high to correctly mimic the physical turbulence decay in turbulent flows. Even the U-MUSCL 2nd order accurate reconstruction procedure does not lead to a sufficiently low dissipation. It has been formally proved that the numerical dissipation introduced by compressible flow schemes does not scale correctly for Mach numbers approaching zero, affecting accuracy. Many approaches have been proposed in the literature to overcome this limitation, and they all fall under the name of *low-Mach number fix(es)*. The original goal of such techniques is reducing the stiffness of the convective terms at low Mach number, as in the boundary layer. Such stiffness is due to the different magnitude of the convective and acoustic flow modes. However, low-Mach fixes are also successful at restoring the accurate behaviour of advective numerical fluxes at low speeds.

One of the easiest approaches to obtain suitable schemes for iLES in the Finite-Volume framework consists in calibrating the numerical dissipation of common shock-capturing schemes, such as the ones based on the Riemann solvers or the Flux Difference Splitting schemes, to match the behaviour of a sub-grid scale model. Generally, Roe numerical convective flux can be written as

$$\bar{F}_c^* = \frac{1}{2}(\bar{F}_L + \bar{F}_R) - \frac{1}{2}|\bar{A}_{\text{Roe}}|(\bar{\Phi}_L - \bar{\Phi}_R) = \frac{1}{2}\bar{F}_{\text{cen}} - \frac{1}{2}|\bar{A}_{\text{Roe}}|\Delta\bar{\Phi} \quad (5)$$

that is equivalent to a central flux, corrected by a dissipation term. The dissipation is computed on the interface jump  $\Delta\bar{\Phi}$  and on the Roe dissipation matrix  $|\bar{A}_{\text{Roe}}|$ .

Two solutions are discussed here. One option is to alter the jump vector  $\Delta\bar{\Phi}$ . This has been proposed by Thornber et al. [31], where the authors redefine the velocity jump as a function of the local Mach

number. In Rieber [32] the velocity jump is simply multiplied by the local Mach number (if  $\text{Ma}_L < 1$ ) and the authors support the method with a rigorous asymptotic analysis of the fix. A second option is to alter the magnitude of the entire dissipation matrix  $|A_{\text{Roe}}|$ , multiplying it by a parameter  $0 \leq c_{\text{diss}} \leq 1$ , as proposed in Amirante and Hills [16] and Camarri et al. [15]. This poses the challenge of specifying  $c_{\text{diss}}$  according to the flow conditions. Bui [33] states that better turbulence predictions with Roe Flux-Difference Splitting (FDS) scheme can only be obtained by scaling down the dissipation by a scalar. Without this correction, the numerical dissipation introduced by Roe scheme is too high and no improvement is obtained with any other method, such as refining the spatial/temporal discretisation or even adopting more accurate time-marching methods. Finally, it is argued that the choice for  $c_{\text{diss}}$  should fall on the minimum value that provides stable calculations.

The approach followed in this research is a hybridisation of the ones discussed above. The dissipation in Roe FDS scheme is indeed multiplied by a scalar coefficient. However, this is not done when computing the numerical flux, but rather when the dissipation matrix ( $\bar{A}_{\text{Roe}}$ ) is assembled. The dissipation term  $\bar{d}$  in Roe numerical flux can be rewritten based on the wave strengths  $\alpha_i$ , the eigenvalues  $\lambda_i$  and the eigenvectors  $\bar{k}^i$ , as shown, among the others, by Boniface [34]

$$\bar{d} = \frac{1}{2}\bar{A}_{\text{Roe}} \cdot \Delta\bar{\Phi} = \sum_{i=1}^5 \alpha_i |\lambda_i| \bar{k}^i \quad (6)$$

The eigenvalues  $\lambda_1 \dots \lambda_5$  depend on the face-normal projected velocity  $u_n$  and the speed of sound  $c$

$$\lambda_1 = u_n - c \quad \lambda_2 = u_n \quad \lambda_3 = u_n \quad \lambda_4 = u_n \quad \lambda_5 = u_n + c \quad (7)$$

where  $\lambda_1$  and  $\lambda_5$  are associated to the non-linear acoustic waves and  $\lambda_2, \lambda_3, \lambda_4$  are associated with the linear entropy and vorticity waves. In the proposed low Mach number fix, the eigenvalues of the Roe matrix are scaled down directly and separately.

The eigenvalues associated with the linear (entropy and vorticity) waves, i.e.  $\lambda_{2,3,4}$ , are simply multiplied by 0, as their contribution to the dissipation can be completely discarded. In fact, vorticity and entropy waves propagate with the local flow velocity and do not introduce significant numerical dissipation in the flow. This is valid under the assumption that the flow does not involve shocks or other compressible flow effects that may require stabilisation. On the other hand, the eigenvalues associated with the non-linear (acoustic) waves  $\lambda_{1,5}$  are multiplied by the scalar coefficient  $c_{\text{diss}}$ . In fact, the dissipation associated with the acoustic waves is relevant and cannot be entirely discarded, as it is essential for the stability of the calculation. Summarising, the eigenvalues are scaled in the following way

$$\bar{\lambda}_1 = \lambda_1 \cdot c_{\text{diss}} \quad \bar{\lambda}_{2,3,4} = 0 \quad \bar{\lambda}_5 = \lambda_5 \cdot c_{\text{diss}} \quad (8)$$

The scalar coefficient  $c_{\text{diss}}$  cannot be set to the minimum value that ensures stability, as it is found that this leads to the dissipation being too low. The coefficient is then calibrated via a set of trial simulations on a fundamental test case, the decay of Homogeneous Isotropic Turbulence. The proposed solution represents an easy and elegant correction that allows the straightforward porting of a traditional Unsteady-RANS solver to the high-fidelity framework. The effectiveness of the resulting numerical scheme in the accurate simulation of turbulence is analysed in the following section.

## 3. Validation and discussion

The numerical setup selected to perform implicit-LES is first verified in terms of order of accuracy on an inviscid test case consisting of a vortex transported in uniform flow. The low-dissipation solver is subsequently calibrated and validated on a set of three prototype turbulent flows of growing complexity, where a reference solution computed with higher fidelity methods (DNS or experiments) is available. The first

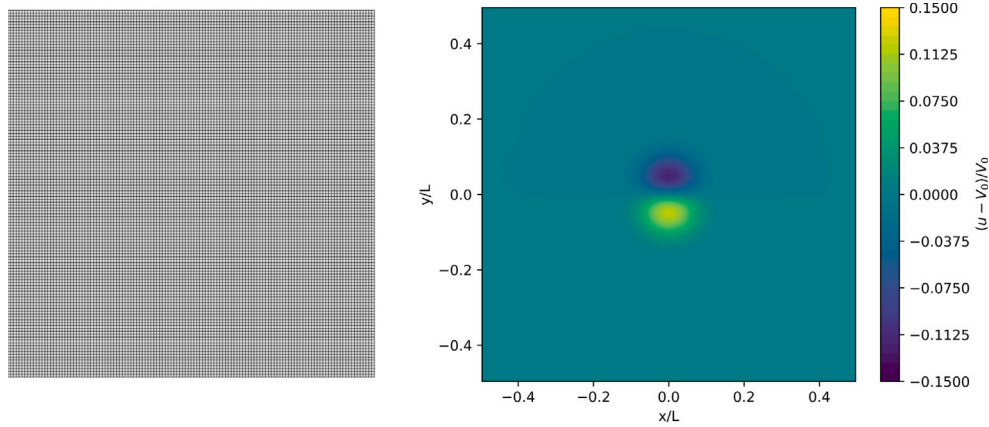


Fig. 1. Vortex transport: computational mesh and initial field ( $u$  velocity) for the mesh LEV1.

(calibration) case is the temporal decay of turbulence in a periodic box, used to assess turbulent dissipation. The second (validation) case is the flow in a periodic channel, computed to evaluate turbulent predictions in the presence of viscous walls. Finally, in a variation of this test case, the periodic channel is used as a turbulent flow generator to feed an asymmetric bump, that includes the effect of wall curvature.

### 3.1. Vortex transport in uniform flow

The correct transport of vorticity by convective mechanisms at all speeds is crucial to get an accurate solution with Large-Eddy Simulation or higher-fidelity turbulent modelling methods [35]. This test case assesses the capability of the solver to properly entrain an isentropic Gaussian vortex in an inviscid, uniform flow. The tested configuration is characterised by a Mach number  $Ma = 0.576$ . Note that in the literature, a low Mach configuration ( $Ma = 0.05$ ) has also been proposed, but a compressible condition has been preferred here, to match the solver nature.

**Mesh and boundary conditions.** The test case consists of a pseudo-2D periodic square domain. The computational domain and mesh (coarsest level  $128^2 \times 2$ ) are shown in Fig. 1. The domain extends  $-\frac{L}{2} \leq x, y \leq \frac{L}{2}$  where the domain side is  $L = 0.1$  m.

The mesh is uniform and only 2 elements are used to discretise the  $z$ -direction. All the sides of the square are periodic, as this reduces the impact of the boundary conditions on the results.

This test case does not rely on the imposition of inlet/outlet boundary conditions and it is rather based on the time-evolution of the initial condition. An isentropic Gaussian vortex of radius  $R_v$  and strength  $\beta$  is placed in the centre of the computational domain ( $X_c, Y_c$ ) at  $t = 0$ . A uniform convective freestream is superimposed to the vortex, with velocity  $V_0$ , temperature  $T_0$  and pressure  $p_0$ . Being the flow uniform and inviscid, the vortex is expected to be rigidly transported across the domain and the periodic boundaries. The initial flow-field is defined by

$$r(x, y, z) = \frac{\sqrt{(x - X_c)^2 + (y - Y_c)^2}}{R_v} \quad (9)$$

$$u(x, y, z) = V_0 \left[ 1 - \beta \frac{y - Y_c}{R_v} \exp\left(\frac{-r^2}{2}\right) \right] \quad (10)$$

$$v(x, y, z) = V_0 \beta \frac{x - X_c}{R_v} \exp\left(\frac{-r^2}{2}\right) \quad (11)$$

$$w(x, y, z) = 0 \quad (12)$$

$$T(x, y, z) = T_0 - \frac{1}{2c_p} (V_0 \beta)^2 \exp(-r^2) \quad (13)$$

$$p(x, y, z) = p_0 \left( \frac{T}{T_0} \right)^{\frac{\gamma}{\gamma - 1}} \quad (14)$$

Table 1

Vortex transport: boundary conditions.

| $\beta$ | 0.2     | [-]   |
|---------|---------|-------|
| $R_v$   | 0.005   | [-]   |
| $V_0$   | 200     | [m/s] |
| $T_0$   | 300     | [K]   |
| $p_0$   | 100 000 | [Pa]  |

Table 2

Vortex transport: mesh element count and characteristic dimension.

| Case | Elem                      | h [m]                |
|------|---------------------------|----------------------|
| LEV1 | $128 \times 128 \times 2$ | $7.81 \cdot 10^{-4}$ |
| LEV2 | $192 \times 192 \times 2$ | $5.21 \cdot 10^{-4}$ |
| LEV3 | $288 \times 288 \times 2$ | $3.47 \cdot 10^{-4}$ |
| LEV4 | $432 \times 432 \times 2$ | $2.31 \cdot 10^{-4}$ |
| LEV5 | $648 \times 648 \times 2$ | $1.54 \cdot 10^{-4}$ |
| LEV6 | $972 \times 972 \times 2$ | $1.03 \cdot 10^{-4}$ |

where  $r$  is the radius,  $u, v, w$  are the velocity components and  $c_p$  is the specific heat at constant pressure. The numerical values involved in the equations are reported in Table 1.

The computational domain and initialisation for the streamwise velocity  $u$  is reported in Fig. 1.

**Results.** The time-dependent Euler equations are solved on the domain for a set number of convective periods (a convective period is  $T_c = \frac{L}{V_0} = 10^{-5}$  s). This is repeated on 6 grid refinement levels (see Table 2 for the number of elements and the characteristic size  $h$ ).

Two numerical setups are tested, a 1<sup>st</sup> and a 2<sup>nd</sup> order scheme. For 1<sup>st</sup> order calculations, a single convective period is considered, due to the extremely high diffusion induced by the numerical scheme. For 2<sup>nd</sup> order calculations, 10 convective periods are considered. The error with respect to the initial condition increases with time, but the asymptotic trend with grid refinement is expected to be unchanged. Hence a different number of  $T_c$  for the two setups can be chosen.

The discretisation error is calculated as the Root-Mean-Square (RMS) of the error between the initial and the computed  $u$  velocity field, non-dimensionalised by  $V_0$ . Results are plotted in Fig. 2.

It can be observed that the error for the 1st order case reduces weakly, with a slope smaller than 1. This is to be ascribed to the unsuitability of the test case to be solved with low-order discretisation methods, as the vortex quickly loses coherency and spreads over the domain. In fact, 1st order tests perform progressively better at low characteristic size, as on the two finest levels the slope increases up to 0.6.

The 2nd order tests show instead a robust behaviour, with the error reducing almost with slope 2 and its magnitude becoming gradually

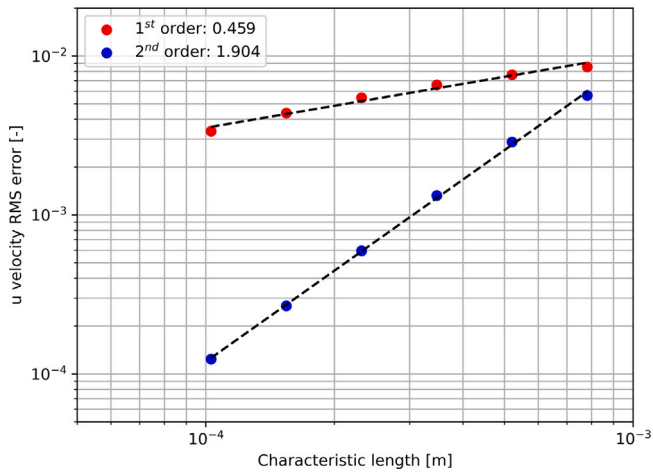


Fig. 2. Vortex transport: asymptotic convergence of the error.

negligible (always lower than 1% and down to 0.01%). Other solution variables show similar behaviour, with the 1st order performing poorly and the 2nd order behaving well. It can be concluded that the U-MUSCL scheme implemented in the solver raises the order of accuracy sufficiently close to a 2nd order.

### 3.2. Isotropic homogeneous turbulence

The homogeneous isotropic turbulence is a simplified model of a turbulent flow, suitable for analytical and numerical studies. Isotropic turbulence implies the invariance of statistical averages to rotation and reflection [36]. Homogeneous turbulence, in addition, implies invariance to translation. This flow condition can be experimentally obtained downstream of a uniform grid.

The time decay of homogeneous isotropic turbulence is based on the transfer of energy between adjacent turbulent length scales from the integral scale to the Kolmogorov scale. The numerical simulation of this problem can hence assess the capability of the solver to correctly predict the turbulent dissipation, without under- or, as more frequently happens, over-estimating it. In this work, the test case will be used to calibrate the low-dissipation coefficient  $c_{\text{diss}}$ . Results are compared between Zephyrus and the open-source code OpenFOAM, as well as against experimental results.

The reference experimental data for this case are provided by Comte-Bellot and Corrsin [37], where several space-time correlation measurements are provided in the turbulent flow behind a uniform grid. The authors provide a set of measured turbulent spectra (1D and 3D) at different time instants. According to Taylor's frozen turbulence hypothesis, the spatial decay of the spectra is converted to a temporal decay using the freestream velocity.

**Model and mesh.** The model consists of a 3D cubic portion of the flow with side  $L = 0.09 \cdot 2\pi$  m, periodic in all directions. The Reynolds number is  $\text{Re} = 34000$ , based on the freestream velocity  $V_0 = 10$  m/s and on the characteristic length scale  $L = 0.0508$  m (i.e. the experimental grid mesh size).

The 3D experimental spectra are available at 3 non-dimensional time instants  $t^* = 42, 98, 171$ , where  $t^* = t \cdot \frac{V_0}{L}$ . The domain is initialised using the spectrum at  $t^* = 42$  and the solution is evolved in time and analysed at  $t^* = 98$  and  $t^* = 171$ . The results are computed on 3 mesh levels, i.e.  $N = 32^3$ ,  $N = 64^3$  and  $N = 128^3$ . The meshes are uniform and perfectly orthogonal. The coarsest level is shown in Fig. 3. In the same figure, the initial  $u$  velocity distribution is represented.

**Initialisation procedure.** The computation of synthetic turbulence starting with a specified 3D spectrum is not trivial. Among the available methods, the one proposed by Saad et al. [38] is selected. The algorithm can be synthesised as follows:

- Given the domain dimensions and grid resolution, a range of solvable wave-numbers is computed and split in bins (or Fourier modes  $\kappa_m$ ).
- An amplitude ( $q_m$ ) is computed for each mode, using the available spectrum  $E(\kappa_m)$ .
- A modal unit wave-number vector is computed ( $\hat{k}_m$ ), using a uniform random distribution. An auxiliary intermediate unit vector ( $\hat{c}_m$ ) is computed and the modal direction vector ( $\hat{\sigma}_m$ ) is computed such that it is perpendicular to both  $\hat{k}_m$  and  $\hat{c}_m$ .
- A random phase ( $\psi_m$ ) is computed from a uniform random distribution.
- The velocity vector is assembled by superimposing the modal information, i.e. the amplitude, the wave-number vector, the phase and the direction vector as in

$$\bar{u}(\bar{x}) = 2 \sum_{m=1}^M q_m \cos(\kappa_m \hat{k}_m \cdot \bar{x} + \psi_m) \hat{\sigma}_m \quad (15)$$

This methodology reproduces the desired spectrum with a *random* velocity field that fulfils the discrete mass conservation equation (i.e. it is divergence-free). The velocity field is computed at the spatial positions corresponding to the cell-centres of the simulated grid. The number of modes used for the modal procedure is  $m = 5000$ .

The initial temperature and pressure fields are uniform and computed such that the desired Reynolds number is obtained. This implies setting the correct kinematic viscosity  $\nu$  and thus the correct density  $\rho$  (being the dynamic viscosity fixed to  $\mu = 1.85 \cdot 10^{-5} \frac{\text{kg}}{\text{m s}}$ ). Consequently, the static temperature is set to  $T = 284.3$  K and the static pressure to  $p = 101325$  Pa (atmospheric).

**Simulation setup.** This case is simulated in Zephyrus as *laminar* with the low-dissipation Roe scheme. The chosen value of the low-dissipation scalar parameter is  $c_{\text{diss}} = 0.001$ . Sensitivity of the turbulence results to the value of  $c_{\text{diss}}$  will be investigated.

The physical timestep is computed from the Courant–Friedrichs–Lewy condition  $\text{CFL} = V_0 \frac{\Delta t}{\Delta x} \approx 0.25$ , where the CFL number is defined on  $V_0$  and on the characteristic size of the finest mesh  $\Delta x = \frac{L}{N}$ . This leads to  $\Delta t = 10^{-4}$  s.

A reference solution is obtained on the same computational domains with the unsteady incompressible solver *pimpleFoam* (from the open-source code OpenFOAM). Gradient, divergence and laplacian schemes are all based on Gaussian integration and linear interpolation (i.e. *Gauss linear*), with a non-orthogonal correction for the laplacian. The turbulence model is WALE LES. A 2nd order backward scheme is adopted for the temporal discretisation, with timestep  $\Delta t = 10^{-3}$  s.

**Post-processing.** In order to compare the results to the experimental data, the 3D energy spectrum must be computed from the velocity field. The procedure is borrowed from McDermott [39]. The (spatial) velocity correlation tensor is defined as

$$R_{ij}(\bar{r}) = \langle u_i(\bar{x} + \bar{r}, t) u_j(\bar{x}, t) \rangle \quad (16)$$

and gathers all the spatial two-point statistics at fixed time. The  $\langle \rangle$  operator is an ensemble average (i.e. an arithmetic mean computed on a large number of samples) and  $\bar{r}$  is the spatial lag or distance. The velocity spectrum tensor  $\Phi_{ij}$  is the Fourier transform of the velocity correlation tensor

$$\Phi_{ij}(\bar{\kappa}) = \frac{1}{(2\pi)^3} \iiint R_{ij}(\bar{r}) e^{-i\bar{\kappa} \cdot \bar{r}} d\bar{r} \quad (17)$$

The energy spectrum is the integral of the spectral energy  $\frac{1}{2} \Phi_{ii}(\bar{\kappa})$  on a spherical shell  $S$  at a radial distance  $\kappa = \|\bar{\kappa}\|$  from the origin in the

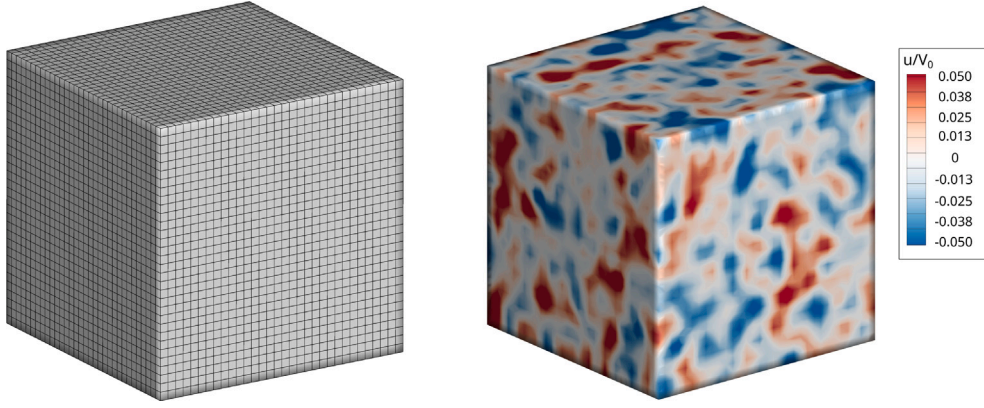


Fig. 3. HIT:  $N = 32^3$  mesh and initialisation ( $u$  velocity).

### 3D Fourier space

$$E(\kappa) = \oint_S \frac{1}{2} \Phi_{ii}(\bar{\kappa}) d\bar{S}(\bar{\kappa}) \quad (18)$$

Since only the diagonal of the velocity correlation tensor is relevant for the computation of the energy spectrum and the ensemble average is commutative with the Fourier transform, in practice the spectral energy can be computed as

$$\frac{1}{2} \Phi_{ii}(\bar{\kappa}) \equiv \frac{1}{2} \hat{u}_i(\bar{\kappa}) \hat{u}_i^*(\bar{\kappa}) \quad (19)$$

where  $\hat{u}_i^*$  is the complex conjugate of  $\hat{u}_i$  and  $1 - \frac{N}{2} \leq \kappa_1, \kappa_2, \kappa_3 \leq \frac{N}{2}$  ( $N$  is the number of points in the  $i$ -th direction). As suggested by McDermott [39], the spherical integral can be reduced to a summation on the wavenumber magnitude  $\kappa = \bar{\kappa} \cdot \bar{\kappa}$

$$E(\kappa) = \sum_{\kappa = \sqrt{\bar{\kappa} \cdot \bar{\kappa}}} \frac{1}{2} \hat{u}_i(\bar{\kappa}) \hat{u}_i^*(\bar{\kappa}) \quad (20)$$

In practice, the wavenumber space has to be partitioned in bins with constant wavenumber magnitude  $\kappa$  and the discrete contributions to the spectral energy have to be accumulated in the corresponding bin. The non-dimensionalisation factor proposed by McDermott [39] is neglected and the adimensionalisation is performed based on  $\kappa_0 = \frac{2\pi}{L}$ .

**Results.** Results are compared between Zephyrus ( $c_{\text{diss}} = 0.001$ ), OpenFOAM and the experimental data in Fig. 4 for all grid levels. Firstly, it is observed that the initial spectrum closely matches the spectrum at  $t^* = 42$  up to the Nyquist wavenumber on all grids. At  $t^* = 98$ , both Zephyrus and OpenFOAM correctly catch the  $-\frac{5}{3}$  slope in the inertial range and they only tend to depart from it when close to the Nyquist threshold. This effect becomes progressively negligible on finer grids, as the Nyquist wavenumber increases. The agreement with the experiments at  $t^* = 171$  is equally satisfactory for both solvers, as the energy decay in the inertial range is well matched. Differences between Zephyrus and OpenFOAM are qualitatively negligible, but it is observed that OpenFOAM tends to be slightly less dissipative.

Results of a sensitivity study on the value of the low-dissipation scalar parameter  $c_{\text{diss}}$  are presented in Fig. 5. Five values of  $c_{\text{diss}}$  are tested on the mesh  $N = 64^3$ , namely  $c_{\text{diss}} = 0.0001, 0.0005, 0.001, 0.002, 0.01$ . The spectra are compared at  $t^* = 98$ . It is evident that values of  $c_{\text{diss}}$  higher than 0.001 lead to an overestimation of the  $-\frac{5}{3}$  slope in the inertial range, with lower turbulence energy levels predicted. Vice-versa, for values lower than 0.001, the curves flatten and the energy close to the Nyquist threshold is overestimated. This suggests that the non-linear wave amplitudes in the Roe scheme cannot be simply set to the smallest value that guarantees stability, as this would spoil the energy decay in the inertial range. Overall, the results on the HIT test case confirm the suitability of the chosen numerical setup (with  $c_{\text{diss}} = 0.001$ ) for the simulation of turbulence, at least from a fundamental flow perspective. Further validation will be carried out on more realistic prototype flows in the following sections.

### 3.3. Turbulent channel flow

The classical test case for the verification and validation of turbulence modelling methodologies for wall-bounded flows is the fully developed channel flow. The domain consists of 2 parallel viscous walls, with periodic streamwise and spanwise boundaries.

In a channel flow the mean shear forces balance the streamwise mean pressure gradient  $\frac{d\tau}{dy} = \frac{dp}{dx} = \text{const}$ . The shear stress profile is linear and antisymmetric in the wall-normal direction and it is independent of the fluid properties (e.g.  $\rho$  and  $\mu$ ).

$$\tau(y) = \tau_w \left(1 - \frac{y}{h}\right) \quad (21)$$

In a channel flow simulation, the streamwise pressure gradient cannot be imposed as a pressure difference between inlet/outlet, due to periodic boundary conditions. However, the same effect can be obtained with a streamwise body force  $\vec{f}_e = f_e \hat{x}$ , whose magnitude depends on the wall shear stress  $\tau_w$

$$f_e = -\frac{dp}{dx} = -\frac{d\tau}{dy} = \frac{\tau_w}{h} \quad (22)$$

The body force is introduced as a source in the momentum and energy equations

$$\frac{\partial \rho \bar{u}}{\partial t} + \nabla \cdot (\rho \bar{u} \times \bar{u}) = -\nabla p + \nabla \cdot \bar{\tau} + \vec{f}_e \quad (23)$$

$$\frac{\partial \rho E}{\partial t} + \nabla \cdot (\rho H) = -\nabla \cdot \bar{q} + \nabla \cdot (\bar{\tau} \cdot \bar{u}) + \vec{f}_e \cdot \bar{u} \quad (24)$$

Working conditions for channel flow simulations are usually identified by the *bulk* and the *friction* Reynolds number, respectively computed on the bulk velocity  $V_b$  and on the friction velocity  $u_\tau$ . In both cases, the channel *half*-height is used as the reference length scale

$$\text{Re}_b = \frac{\rho V_b h}{\mu} \quad \left(V_b = \int_A V dA\right) \quad \text{Re}_\tau = \frac{\rho u_\tau h}{\mu} \quad \left(u_\tau = \sqrt{\frac{\tau_w}{\rho}}\right) \quad (25)$$

The flow in a plane channel is expected to be turbulent for  $\text{Re}_b > 900$  and residual transitional effects become negligible for  $\text{Re}_b > 1500$ . Note that  $\text{Re}_\tau$  is the ratio of the channel *half*-height to the viscous length  $\text{Re}_\tau = \frac{h}{\delta_v}$ , where the viscous length is the relevant length-scale near the wall  $\delta_v = \frac{\nu}{u_\tau}$ . The body force magnitude can hence be directly related to the friction Reynolds number

$$f_e = \frac{\tau_w}{h} = \frac{\rho u_\tau^2}{h} = \text{Re}_\tau^2 \frac{\mu^2}{\rho h^3} \quad (26)$$

The working condition for a channel flow simulation is only determined by the body force  $f_e$  and by the initial gas state ( $p, T$ ), the latter based on the desired Reynolds and Mach number. As analytically shown by Pope [40], a relation exists between  $\text{Re}_b$  and  $\text{Re}_\tau$ . The values selected for the present simulations are  $\text{Re}_b = 3173$  and  $\text{Re}_\tau = 200$  from the reference DNS in Banchetti et al. [41].

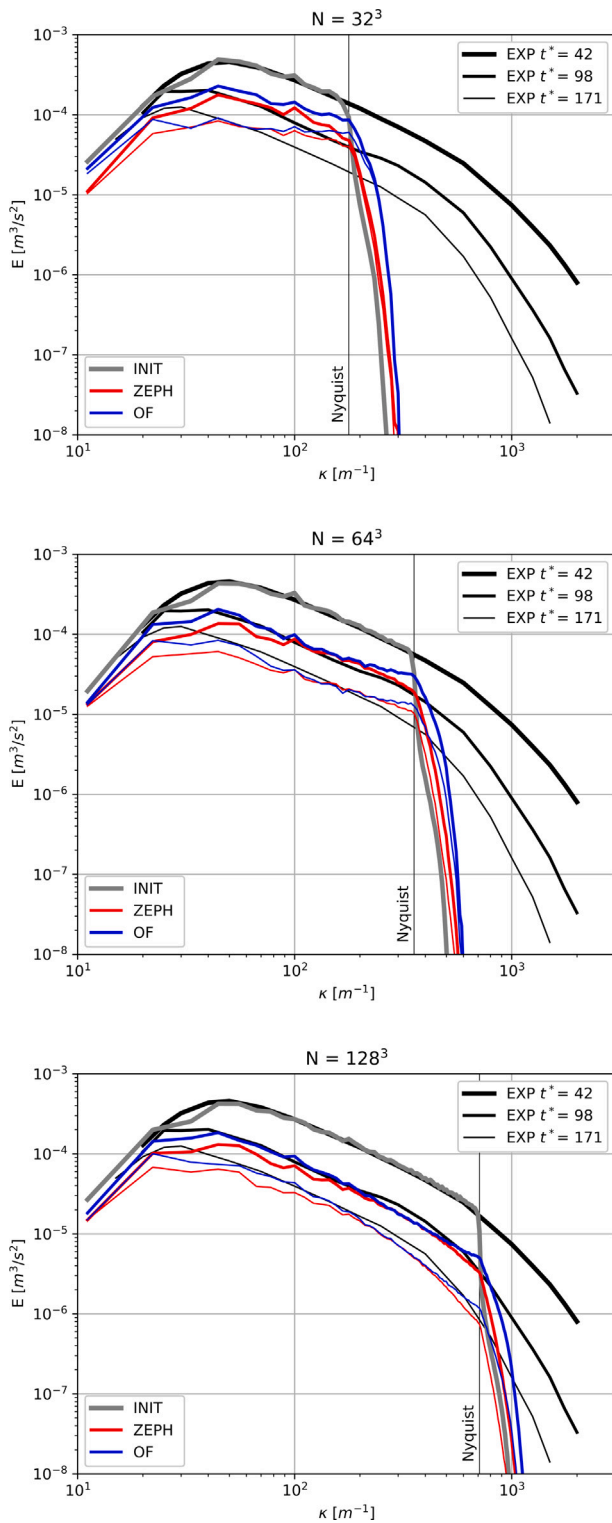


Fig. 4. HIT: turbulence spectra for mesh levels  $N = 32^3$ ,  $N = 64^3$ ,  $N = 128^3$  and  $c_{\text{diss}} = 0.001$ .

In a turbulent channel flow, fluctuations  $(u', v', w')$  appear on all velocity components  $(u, v, w)$ . Note that  $\langle v \rangle = 0$  must be verified to match the mean continuity equation and  $\langle w \rangle = 0$  has to be true for symmetry reasons. A fully developed turbulent channel flow is statistically stationary and statistically 1D in the wall-normal direction  $y$ . Moreover, the flow is statistically symmetric about the mid-plane

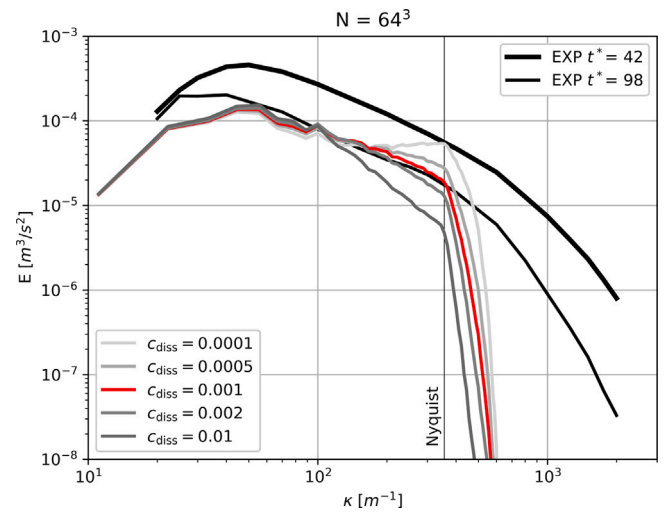


Fig. 5. HIT: turbulence spectrum sensitivity to  $c_{\text{diss}}$ .

Table 3

Channel flow: working conditions.

|            |                     |                      |
|------------|---------------------|----------------------|
| $Re_\tau$  | [-]                 | 200                  |
| $u_\tau$   | [m/s]               | 3.12                 |
| $\delta_v$ | [m]                 | $5.00 \cdot 10^{-6}$ |
| Ma         | [-]                 | 0.143                |
| $V_b$      | [m/s]               | 49.54                |
| $f_c$      | [N/m <sup>3</sup> ] | 11552.7              |

$y = h$  implying that the statistics of  $(u, v, w)$  at  $y = y_0$  match the statistics of  $(u, -v, w)$  at  $y = 2h - y_0$ .

**Case setup.** The domain is sized according to the values reported in Banchetti et al. [41]. The streamwise, wall-normal and spanwise dimensions are  $L = 12h$ ,  $H = 2h$ ,  $W = 4h$ . Streamwise and spanwise boundaries are periodic. Upper and lower walls are isothermal with  $T = 298$  K. The mesh is dimensioned based on the viscous length  $\delta_v$  (see Table 3). Spacings at the centreline are  $\Delta x^+ = \frac{\Delta x}{\delta_v} = 15$ ,  $\Delta y^+ = \frac{\Delta y}{\delta_v} = 7.5$ ,  $\Delta z^+ = \frac{\Delta z}{\delta_v} = 10$ , with  $y^+ = 0.5$ . The mesh contains about  $1.2 \cdot 10^6$  elements.

Working conditions are reported in Table 3. A channel flow simulation achieves fully developed conditions regardless of the initialisation. However, Piomelli [4] argue that superimposing random noise to the initial mean velocity profile can substantially speed up the transient. Random perturbations tend to be damped quickly by viscosity, hence the noise amplitude must be high (30%) to avoid relaminarisation.

Two time scales are relevant in a channel flow simulation. The bulk period  $t_b = \frac{h}{V_b}$  and the friction period  $t_h = \frac{h}{u_\tau}$ . The flow must fully develop before statistics can be collected. A common rule is  $t > 200t_b$  [4]. However,  $100t_b$  is often enough for the flow to be fully established. Once the flow is statistically stationary, the solution can be sampled. A sufficient sample spacing is needed to guarantee data decorrelation and speed up statistical convergence. Samples are separated by about  $0.2t_h$  timesteps and averaging is performed for about  $10t_h$ .

The simulation timestep can be computed from the condition  $CFL = V_b \frac{\Delta t}{\Delta x} = 0.3$ , based on the bulk velocity  $V_b$  and the streamwise cell spacing  $\Delta x$ . The adopted CFL condition is more restrictive than it is commonly found in the literature (where often  $CFL > 1.5$ ), but this choice is consistent with the value used for the decay of Homogeneous Isotropic Turbulence ( $CFL = 0.25$ ). Table 4 summarises all the relevant temporal scales.

**Table 4**  
Channel flow: characteristic temporal scales.

|            |                        |
|------------|------------------------|
| $\Delta t$ | $5.00 \cdot 10^{-7}$ s |
| $t_b$      | $40\Delta t$           |
| $t_h$      | $640\Delta t$          |
| Transient  | $8000\Delta t$         |
| Spacing    | $128\Delta t$          |
| Sampling   | $6400\Delta t$         |

**Time-resolved results.** Instantaneous contours of velocity on a spanwise mid-plane and on a wall-normal plane at  $y^+ = 20$  are presented in Fig. 6. The lack of momentum close to the viscous wall is the typical signature of a wall-bounded turbulent flow. Fluctuations can be seen in the three velocity components. Turbulent streaks tend to be more elongated close to the wall, especially for the z-velocity ( $w$ ). The fluctuation magnitude is  $\approx 0.1V_b$ .

**Time-averaged results.** The channel length and width must be sufficiently large for the turbulent structures to develop in their full-length before hitting the periodic boundaries and being constrained. The flow in a domain not wide enough relaminarises quickly, or shows bad statistical properties. Due to the streamwise elongation of the streaks close to the wall, the streamwise periodicity is critical. However, close to the channel centreline, the spanwise dimension of the domain becomes equally important.

The domain size can be assessed based on the 2-point velocity autocorrelations, i.e. the diagonal of  $R_{i,j}$  as defined in Eq. (16). Plots of  $R_{11}$ ,  $R_{22}$  and  $R_{33}$  are presented in Fig. 7 for a streamwise (left) and a spanwise (right) spatial lag. The wall-normal position is  $y^+ = 20$  for the streamwise correlations and  $y^+ = 200$  for the spanwise correlations. The streamwise correlations reach almost zero even very close to the wall, where the turbulent streaks are elongated. The spanwise correlations are even better behaved. This implies that the domain length  $L$  and width  $W$  are entirely appropriate.

Being a turbulent channel flow statistically stationary and homogeneous in the streamwise and spanwise directions, averages in  $t$ ,  $x$  and  $z$  must be worked out. As a general rule, averaging is carried out *after* the field of interest has been computed on the full 3D domain and for each timestep. As the statistics are typically deemed to have a weak dependence on the friction Reynolds number, DNS data available for a lower friction Reynolds number ( $Re_\tau = 180$ ) are used for comparison.

The velocity profile in a turbulent channel flow is flatter at the centreline and steeper close to the wall, compared to the laminar case (parabolic). This is due to the cross-mixing induced by the turbulent fluctuations and results in a bulk-to-centreline velocity ratio much lower than 1.5 (laminar). For the present case, the incompressible DNS from Banchetti et al. [41] predicts  $\frac{u(h)}{V_b} = 1.168$ , close to the output of Dean's correlation  $\frac{u(h)}{V_b} = 1.28 Re_b^{-0.0116} = 1.156$ . The iLES value is  $\frac{u(h)}{V_b} = 1.186$ , and it is 3% higher than the reference value.

The velocity profile on half-channel can be seen in Fig. 8 (left). The computed velocity is in excellent agreement with the DNS, with a maximum 3% overestimation at the centreline. This is consistent with the overestimation of the ratio  $\frac{u(h)}{V_b}$  and can be related to an underestimation of the bulk velocity  $V_b$  (and of the bulk Reynolds number  $Re_b$ ).

The velocity-defect law represents the difference between the local average velocity  $\langle u \rangle$  and the centreline velocity  $u(h)$  along the wall-normal direction. The velocity-defect is expected to follow a log-law for  $y^+ > 30$  [40]

$$\frac{u(h) - \langle u \rangle}{u_\tau} = -\frac{1}{\kappa} \log\left(\frac{y}{h}\right) + B_1 \quad (B_1 = 0.2) \quad (27)$$

Fig. 8 (right) shows a comparison between the computed velocity defect and the DNS. The log-law is included as well. The iLES and the DNS are

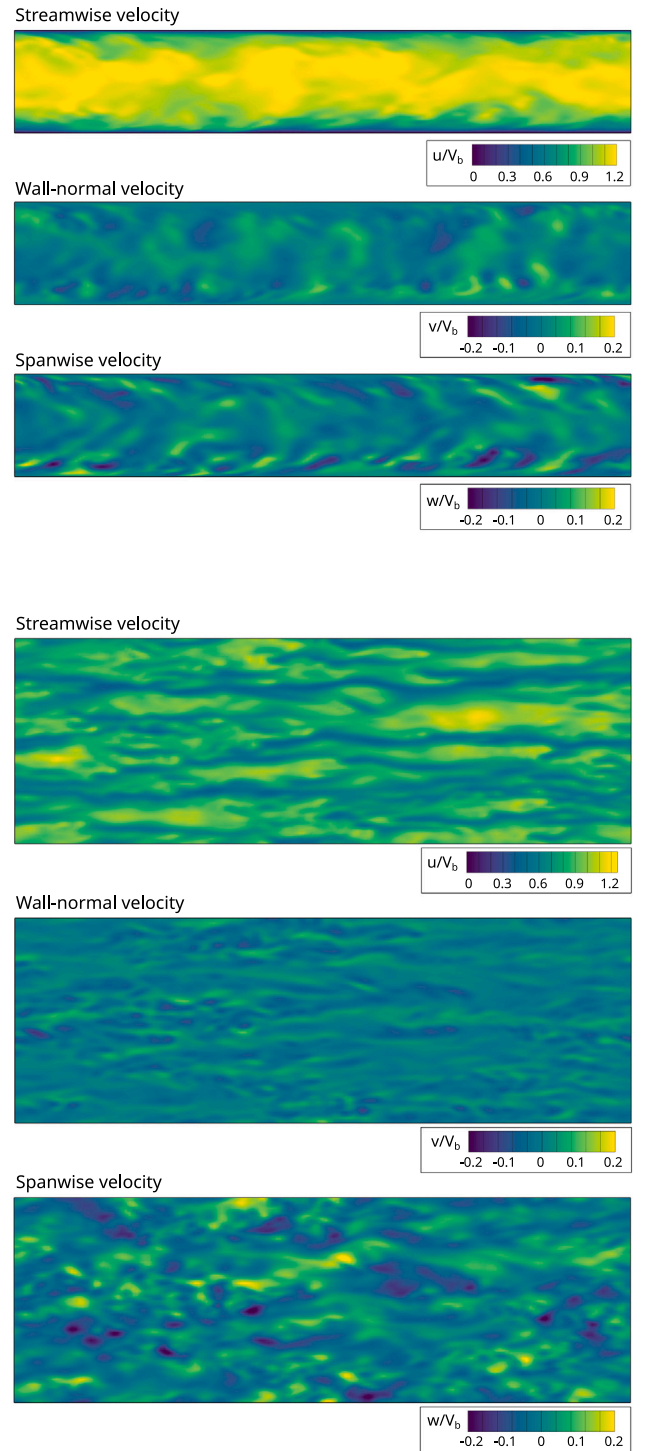


**Fig. 6.** Channel flow: instantaneous velocity contours on a plane  $z = W/2$  (top) and  $y^+ = 20$  (bottom).

in excellent agreement. As expected, a departure of the computational results from the log-law is observed at low  $\frac{y}{h}$ .

A plot of the computed near-wall profile is shown in Fig. 9 (left) and compared between Zephyrus and the DNS. As expected, the iLES mesh does not reach values of  $y^+$  as small as the DNS. Usually, an overestimation of  $u^+$  in the logarithmic layer indicates too high numerical dissipation and an underestimation of  $\tau_w$ . In this case, the profiles agree very well, with only a 2% overestimation of  $u^+$  by the iLES at  $y^+ = 100$  and the boundary layer is correctly modelled.

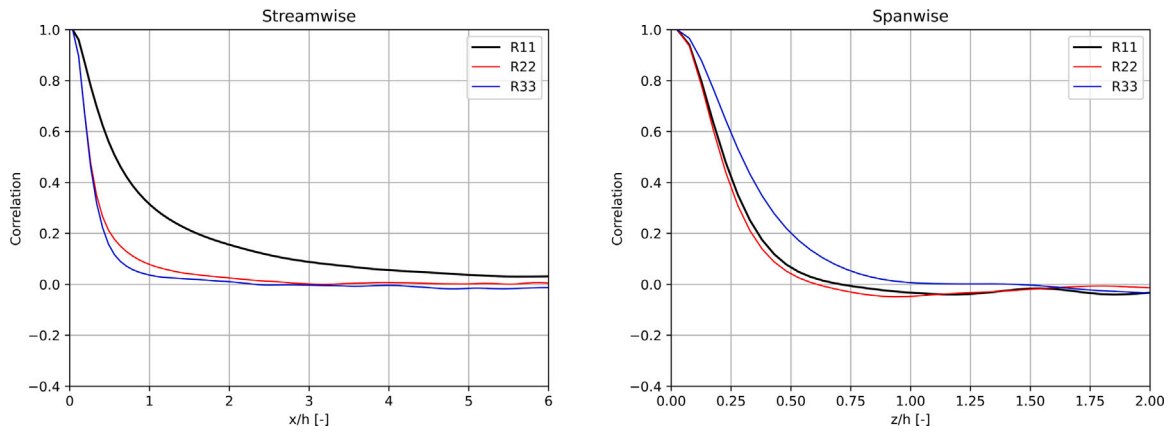


Fig. 7. Channel flow: 2-point correlations streamwise at  $y^+ = 20$  (left) and spanwise at  $y^+ = 200$  (right).

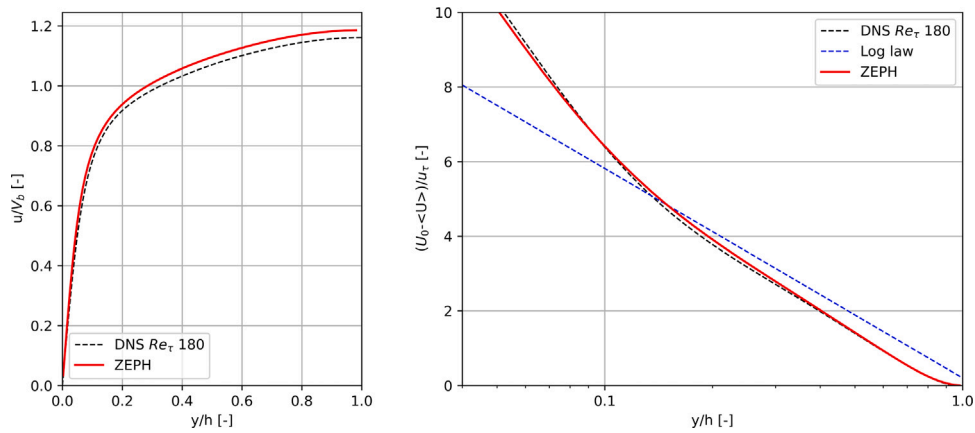


Fig. 8. Channel flow: averaged velocity profile (left) and mean velocity defect (right).

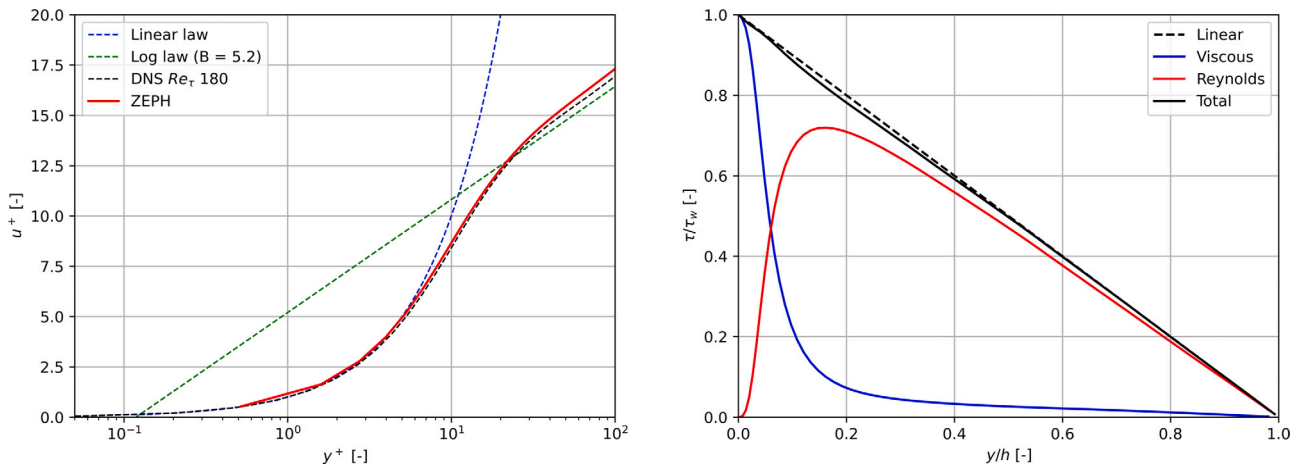


Fig. 9. Channel flow: near-wall profile of velocity (left) and shear stress (right).

For a turbulent flow, there are a laminar and a turbulent contribution to the total shear stress. However, the total shear stress must still be linear with  $y$  as prescribed by Eq. (21). Newton's constitutive law models the laminar part, whereas the Reynolds shear stress contributes to the turbulent part

$$\tau = \mu \frac{d\langle u \rangle}{dy} - \rho \langle uv \rangle \quad (28)$$

Fig. 9 (right) shows the profiles of viscous, Reynolds and total shear stress with  $\frac{y}{h}$ . The laminar stress is the only contribution to the total stress at the wall, as the fluctuations decay to zero. However, the laminar stress reduces quickly out of the viscous sublayer (i.e. for  $y^+ > 5$ ) and the Reynolds stress  $\langle uv \rangle$  contributes mostly to the total shear stress in the buffer and in the logarithmic layer. Deviations from the linear law normally indicate an incomplete statistical convergence of the samples but this issue is negligible in this case.

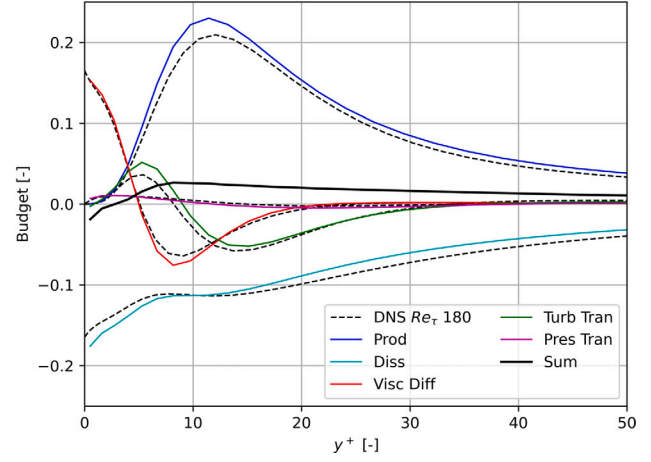
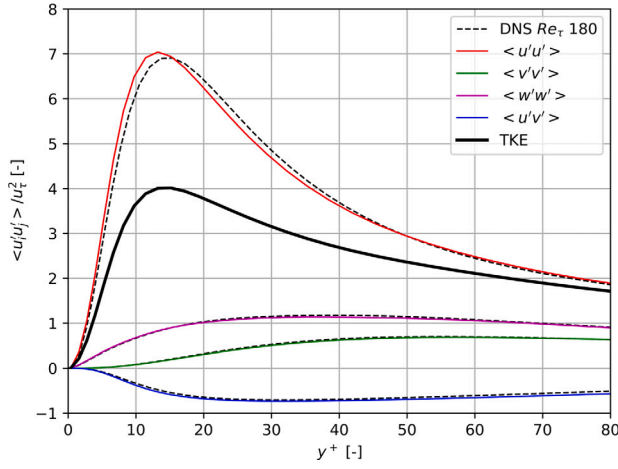


Fig. 10. Channel flow: wall-normal profiles of Reynolds stresses (left) and TKE budgets (right).

**Turbulence statistics.** The Reynolds stress tensor gathers the ensemble average of the velocity fluctuations  $R_{ij} = \langle u'_i u'_j \rangle$ . The most relevant Reynolds stresses for the channel flow case are the ones on the diagonal ( $\langle u'u' \rangle$ ,  $\langle v'v' \rangle$ ,  $\langle w'w' \rangle$ ) and the turbulent shear stress  $\langle u'v' \rangle$  which transfers momentum in the wall-normal direction. Wall-normal profiles of these stresses are reported in Fig. 10 (left). Note that, due to the incompressibility of the test case, a Reynolds decomposition of the flow-field is performed, rather than a Favre decomposition. Turbulent activity is maximum close to the wall, right outside of the viscous sublayer and peaks of turbulence are achieved at  $y^+ < 20$ . The turbulent kinetic energy  $k$  follows the same trend. The streamwise stress  $\langle u'u' \rangle$  is always expected to have a higher magnitude than the others. Overestimation of the streamwise stress indicates excessive numerical dissipation, which seems to be marginally the case here.

The mean flow kinetic energy  $\langle E_k \rangle$  can be split according to a standard Reynolds decomposition on velocities  $\bar{u} = \langle \bar{u} \rangle + \bar{u}'$

$$\langle E_k \rangle = \frac{1}{2} \bar{u} \cdot \bar{u} = \frac{1}{2} \langle \bar{u} \rangle \cdot \langle \bar{u} \rangle + \frac{1}{2} \bar{u}' \cdot \bar{u}' = E_{k,avg} + k \quad (29)$$

where  $E_{k,avg}$  is the average kinetic energy and  $k$  is the turbulent kinetic energy. A balance equation (*turbulence budgets*) can be written for the turbulent kinetic energy

$$0 = P - \tilde{\epsilon} + \nu \frac{d^2 k}{dy^2} - \frac{d}{dy} \left( \frac{1}{2} v' (\bar{u}' \cdot \bar{u}') \right) - \frac{1}{\rho} \frac{d}{dy} \langle v' p' \rangle \quad (30)$$

where production and pseudo-dissipation are respectively defined as

$$P = -\langle u_i u_j \rangle \frac{\partial u_i}{\partial x_j} \quad \tilde{\epsilon} = \frac{\mu}{\rho} \left\langle \frac{\partial u'_i}{\partial x_j} \frac{\partial u'_i}{\partial x_j} \right\rangle \quad (31)$$

Budgets for the iLES solution are compared to the DNS in Fig. 10 (right). All values are non-dimensionalised by the reference quantity  $\frac{\rho u_\tau^4}{\mu}$ .

The production term  $P$  reaches its peak in the buffer layer, where  $y^+ \approx 12$  and around here production exceeds pseudo-dissipation  $\tilde{\epsilon}$  and turbulence is generated. Turbulent dissipation is maximum at the wall, as the fluctuating strain rate does not vanish, even if the turbulent kinetic energy is zero. The dissipation at the wall is balanced by viscous transport  $\nu \frac{d^2 k}{dy^2}$  which conveys turbulent kinetic energy towards the wall. Turbulent convection  $\frac{d}{dy} \left( \frac{1}{2} v' \bar{u}' \cdot \bar{u}' \right)$  transports energy in both directions, towards and away from the wall. The last term in the equation is pressure transport  $\frac{1}{\rho} \frac{d}{dy} \langle v' p' \rangle$ . All terms disappear moving towards the centreline, except production and dissipation which eventually balance at  $y = h$ . The agreement between iLES and DNS is qualitatively good, although some differences in peak amplitudes can be seen. These can be ascribed to the discrepancy in  $Re_\tau$  and to the isothermal wall condition, that creates a non-uniform temperature and viscosity field.

Summarising, the results obtained on the turbulent channel flow are in excellent agreement with the reference DNS data. The iLES

Table 5  
Turbulent bump: geometric parameters.

| $a$ [-]              | $b$ [m]           | $c$ [m]               | $a'$ [-]               | $b'$ [m]             | $c'$ [m]              |
|----------------------|-------------------|-----------------------|------------------------|----------------------|-----------------------|
| $5.05 \cdot 10^{-5}$ | $4 \cdot 10^{-3}$ | $2.922 \cdot 10^{-4}$ | $6.0425 \cdot 10^{-5}$ | $4.36 \cdot 10^{-3}$ | $3.847 \cdot 10^{-4}$ |

solver is capable of matching the near-wall turbulent production and dissipation to a very good extent. A minor overestimation of the trend in the logarithmic layer region suggests that the solver is still slightly over-dissipative, but this appears as a minor effect.

### 3.4. Bump

The final step on the way of validating the iLES methodology implemented in Zephyrus consists in testing it on a non-planar turbulent channel flow. This poses several challenges to the solver, including the capability of preserving accuracy in the presence of non-orthogonal cells. The reference data for this case is enclosed in Banchetti et al. [41]. The turbulent channel flow simulated in the previous section is used as a turbulence generator for the bump and hence placed upstream of the bump domain. The upper and lower walls are isothermal with  $T = 298$  K.

The computational domain is shown in Fig. 11 and consists of a flat wall channel (upstream) and a curved wall channel with a 2D bump (downstream). The streamwise, wall-normal and spanwise dimensions match exactly the ones for the turbulent channel, respectively  $L = 12h$ ,  $H = 2h$ ,  $W = 4h$ , where  $h$  is the channel half-height. The 2D equation for the bump wall consists of 2 superimposed Gaussian curves

$$y(x) = a \exp \left[ - \left( \frac{x-b}{c} \right)^2 \right] + a' \exp \left[ - \left( \frac{x-b'}{c'} \right)^2 \right] \quad (32)$$

where the geometrical parameters ( $a$ ,  $b$ ,  $c$ ,  $a'$ ,  $b'$ ,  $c'$ ) are reported in Table 5. The resulting bump height is  $\frac{h_b}{h} = 0.0837$  at  $\frac{x}{h} = 4.14$ . The bump is not symmetric and the section downstream of the tip is stretched with a streamwise expansion factor of 2.5.

**Case setup.** This test case inherits all the working conditions from the upstream turbulent channel, including the bulk and the friction Reynolds numbers  $Re_b = 3173$  and  $Re_\tau = 200$  (see Table 3). The solver setup is the same as for the turbulent channel simulation and indeed the same timestep and temporal scales are adopted for flow development and sampling (Table 4). The two domains are coupled with a 1-to-1 matching boundary condition allowing the flow field at the channel output to be used as the bump input condition. Meanwhile, the channel keeps working in a periodic way. The bump outlet is a characteristic exit condition with constant pressure  $p = 101450$  Pa. This value must

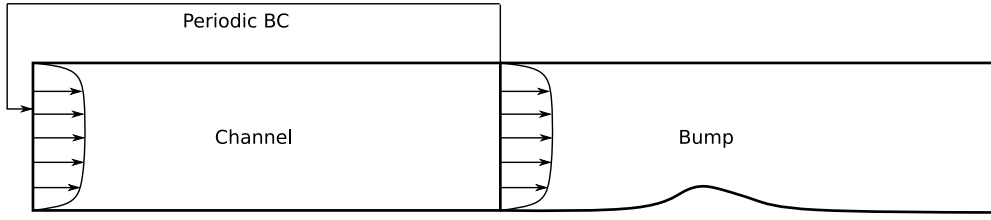
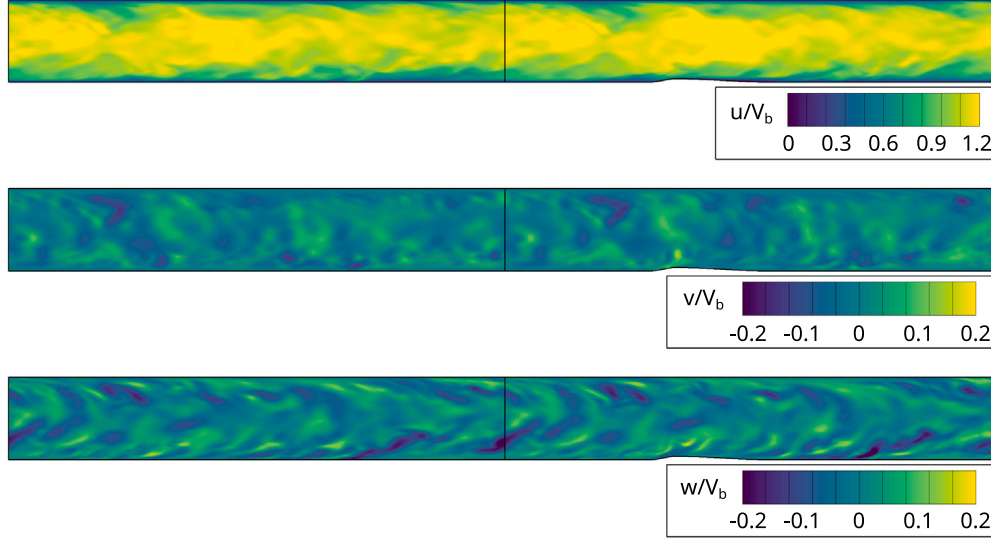


Fig. 11. Turbulent bump: domain schematic.

Fig. 12. Turbulent bump: instantaneous velocity contours on a plane  $z = W/2$ .

be carefully chosen, accounting for the pressure drop in the bump, to ensure that the temperature and pressure at the bump inlet are (on average) matching the channel flow outlet.

A reference solution is obtained in OpenFOAM with a setup similar to the one used for the HIT test case. Gradient, divergence and laplacian schemes are all based on Gaussian integration and linear interpolation (i.e. *Gauss linear*), with a non-orthogonal correction for the laplacian. The turbulence model is in this case LES with the k-equation SGS model. A 2<sup>nd</sup> order backward scheme is adopted for the temporal discretisation. Statistic convergence and averaging are evaluated with a rationale similar to the one adopted for Zephyrus.

The mesh in the  $y$  and  $z$  direction corresponds to the one for the turbulent channel, to ensure exact matching at the boundaries. The  $x$  spacing is not constant and the mesh is refined in the streamwise direction in the higher curvature regions. In particular,  $\Delta x$  reduces from a value  $\Delta x^+ = 15$  at the inlet/outlet to  $\Delta x^+ = 4$  at the bump tip (the refinement factor is  $\approx 4$  and it is the same proposed by Banchetti et al. [41]).

**Time-resolved results.** Instantaneous contours of the three velocity components are shown in Fig. 12. The channel/bump coupling interface is highlighted by a black vertical line. It can be seen how the velocity pattern in the upstream part of the bump is substantially the same as in the upstream region of the channel, as the periodic boundary is feeding both inlets. However, the curved lower wall in the bump domain alters the turbulent streak pattern, inducing an increase in turbulent activity downstream of the bump.

The increase in turbulence across the bump is more evident in Fig. 13, where the instantaneous iso-surfaces of Q-criterion are plotted and coloured by the vorticity magnitude  $\Omega$ . The definitions of vorticity tensor ( $\bar{\bar{\Omega}}$ ), strain-rate tensor ( $\bar{\bar{S}}$ ) and scalar  $Q$  are recalled here

$$\bar{\bar{\Omega}} = \frac{\nabla\bar{u} - \nabla\bar{u}^T}{2} \quad \bar{\bar{S}} = \frac{\nabla\bar{u} + \nabla\bar{u}^T}{2} \quad Q = \frac{1}{2}(\|\bar{\bar{\Omega}}\|^2 - \|\bar{\bar{S}}\|^2) \quad (33)$$

where the scalar  $Q$  represents the second invariant of the velocity gradient tensor. The Q-criterion defines  $Q > 0$  as the condition for the existence of a vortex, i.e. regions where the vorticity magnitude is higher than the rate of strain. Larger values of  $Q$  indicate higher vortex intensities. Note that the vorticity magnitude  $\Omega$  is non-dimensionalised by the reference value  $\frac{V_b}{L}$  (with units  $[s^{-1}]$ ) and the Q-criterion by its square  $(\frac{V_b}{L})^2$ .

**Time-averaged results.** The time-averaged results and turbulence statistics computed in Zephyrus are compared to a reference incompressible DNS and OpenFOAM. Note that, as in the channel flow, due to the incompressibility of the test case, a Reynolds decomposition of the flow-field is performed, rather than a Favre decomposition.

The relevant aerodynamic forces for this test case are pressure and friction. The streamwise profile of pressure coefficient  $C_p$  in the bump domain is compared to the reference DNS [41] and to OpenFOAM in Fig. 14.  $C_p$  is defined as

$$C_p(x) = \frac{\langle p(x) - p_{out} \rangle}{\frac{1}{2}\rho V_b^2} \quad (34)$$

where  $p_{out}$  is the time-averaged pressure averaged on the bump outlet plane. The pressure locally increases upstream of the bump and then a quick expansion takes place, leading to a deep minimum at the bump tip. The profile is not symmetric due to the non-symmetric geometry of the bump itself and a recompression develops downstream the bump tip. Globally, a linear decrease in pressure can be detected from inlet to outlet, implying a constant mean pressure gradient, as expected in a channel flow. The agreement between Zephyrus, OpenFOAM and the DNS is excellent (note that the OpenFOAM results are practically coincident with the DNS). The iLES result only shows a small upstream migration of the positive pressure peak and a 6% overestimation of the negative pressure peak at the bump tip.

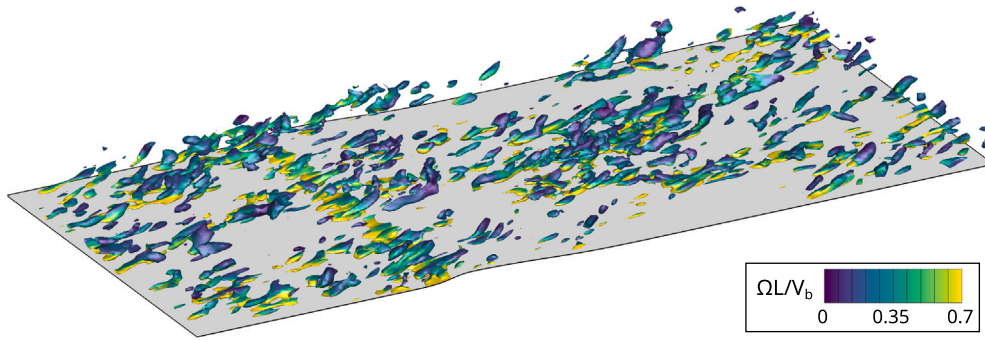


Fig. 13. Turbulent bump: instantaneous iso-surfaces of Q-criterion ( $Q(\frac{L}{V_b})^2 = 3 \cdot 10^{-4}$ ) coloured by vorticity magnitude  $\Omega$ .

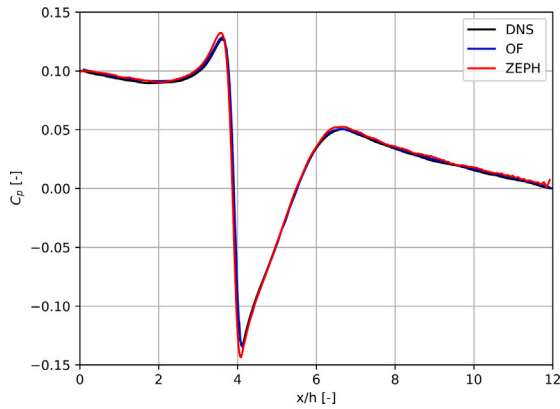


Fig. 14. Turbulent bump:  $C_p$  distribution.

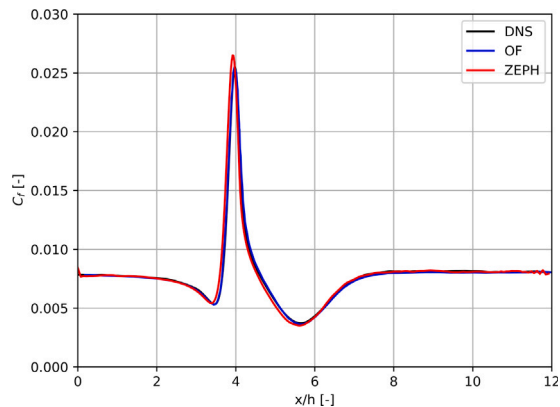


Fig. 15. Turbulent bump:  $C_f$  distribution.

The streamwise distribution of skin friction coefficient  $C_f$  along the lower wall is compared to the reference DNS [41] in Fig. 15.  $C_f$  is defined as

$$C_f(x) = \frac{\langle \tau_w(x) \rangle}{\frac{1}{2} \rho V_b^2} \quad (35)$$

The skin friction coefficient decreases just before the bump and then suddenly spikes at the bump tip, with a maximum value approximately 3-times bigger than that at the flat wall. The flat wall value can be computed from the turbulent channel flow theory as  $C_f = 2(\frac{u_\tau}{V_b})^2 = 7.93 \cdot 10^{-3}$  (well matched). Downstream the tip  $C_f$  quickly drops, but without reaching  $C_f = 0$ , i.e. the flow does not separate. The agreement between the iLES, OpenFOAM and the DNS is again excellent, with only a 4% overestimation of the friction coefficient peak in the iLES.

Moreover, the value of  $C_f$  on the flat wall regions is perfectly in agreement with the DNS.

Finally, the wall-normal profiles of Reynolds stresses at 3 streamwise locations (2 upstream and 1 downstream the bump tip) is compared between the iLES and OpenFOAM in Fig. 16. DNS data are not available for the turbulent fluctuations, but the OpenFOAM solution is considered sufficiently accurate to provide a guideline. The diagonal fluctuations  $\langle u'u' \rangle$ ,  $\langle v'v' \rangle$  and  $\langle w'w' \rangle$  are symmetric with respect to the centreline, while the turbulent shear  $\langle u'v' \rangle$  shows an anti-symmetric behaviour. All profiles show a slight increase in the peak magnitude close to the bottom wall across the bump, confirming the increase in turbulent activity induced by the curved wall. All iLES profiles agree reasonably well with OpenFOAM. Some slight underestimation can be seen in  $\langle v'v' \rangle$  and  $\langle w'w' \rangle$ .

In conclusion, results on this test case show that the iLES achieves an accuracy comparable to the DNS and to OpenFOAM. Note that OpenFOAM runs an incompressible solver with a substantially more sophisticated SGS model (k-equation). The averaged quantities (pressure and friction coefficient) match almost perfectly between the iLES and the reference data. Minor deviations are observed for turbulent fluctuations. This can be ascribed to the higher numerical dissipation induced in the iLES by the mesh non-orthogonality and non-uniformity in the streamwise direction.

#### 4. Conclusions

An implicit-LES methodology has been implemented and validated in an existing compressible Finite-Volume URANS solver for the Navier–Stokes equations. The wall-resolved iLES model allows to run high-fidelity simulations without the use of a sub-grid scale model. A modified version of the classical Roe FDS scheme is required to match the numerical dissipation of the CFD to that of the unresolved turbulence scales.

- The solver accuracy has been tested on the fundamental case of vortex transport in uniform flow and the expected 2<sup>nd</sup> order trend is observed. It is subsequently shown that a 2<sup>nd</sup> order accurate numerical scheme is sufficient for the iLES simulation of turbulence. The use of lower-dissipation or higher-order schemes (e.g. low-dissipation AUSM schemes or k-exact reconstruction for Finite-Volume methods) could be justified for specific applications, but has not proved essential for the investigated test cases.
- The solver dissipation has to be reduced, in order for turbulence to be properly modelled. This has required a rescaling of the eigenvalues in Roe FDS scheme. In particular, linear wave amplitudes have been set to zero and acoustic wave amplitudes have been scaled with a scalar coefficient  $c_{\text{diss}} = 0.001$ .
- The value of the coefficient  $c_{\text{diss}}$  has been calibrated to match the decay of Isotropic Homogeneous Turbulence. The dissipation scaling procedure is found to reproduce the physical behaviour of turbulence in an accurate way (within the Nyquist limit).

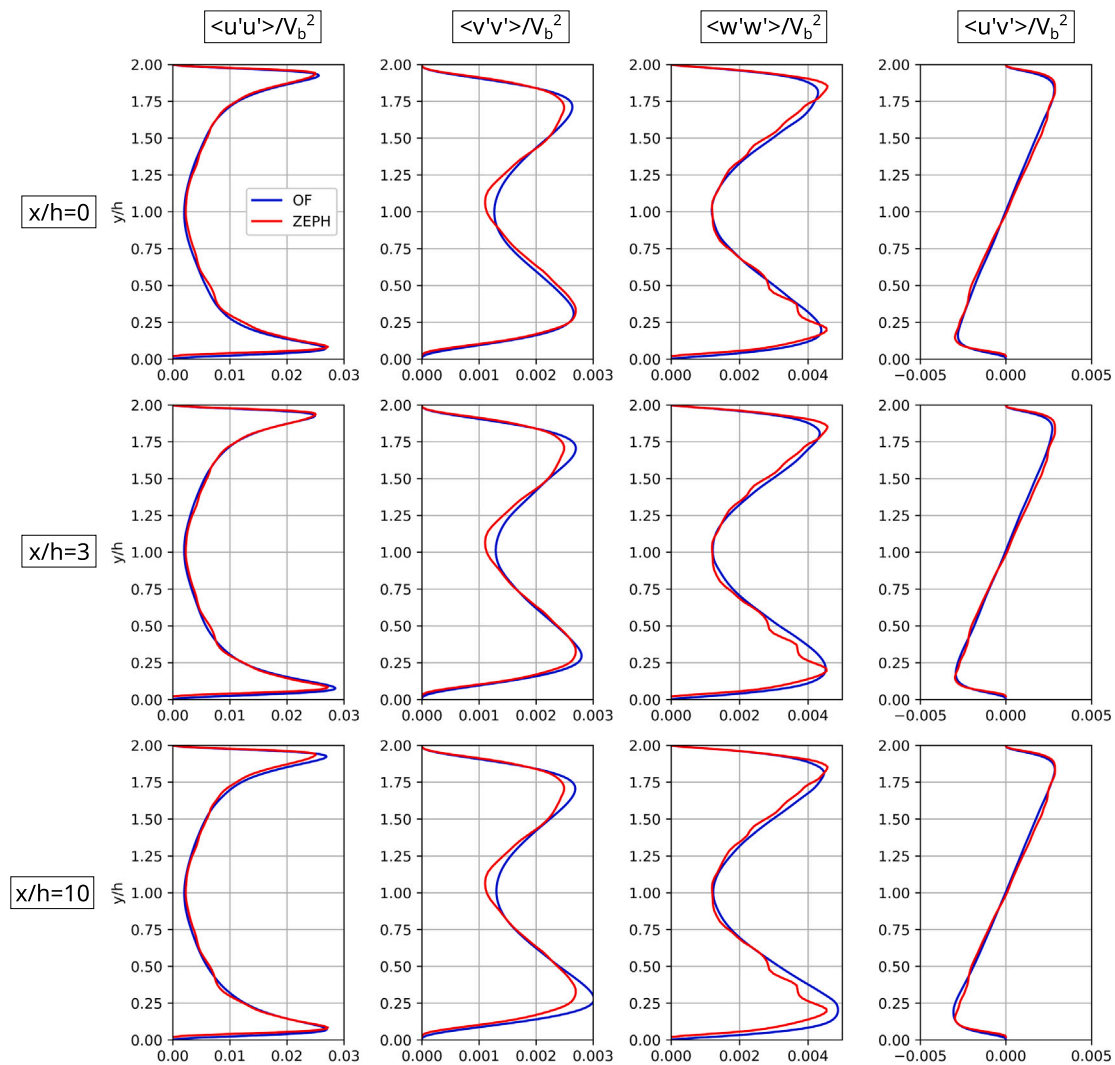


Fig. 16. Turbulent bump: wall-normal profiles of Reynolds stresses at 3 streamwise locations:  $x/h = 0$ ,  $x/h = 3$  (upstream bump tip) and  $x/h = 10$  (downstream bump tip).

- The implementation has been validated on prototype flows, namely a turbulent channel and a turbulent bump. Results show that the calibration carried out on a simple test case leads to accurate modelling of turbulence in more complex test cases. This is an easy and elegant solution for the implementation of an implicit-LES module in a classic URANS Finite-Volume CFD solver.

#### CRediT authorship contribution statement

**Giove De Cosmo:** Writing – review & editing, Writing – original draft, Validation, Software, Methodology, Formal analysis, Data curation, Conceptualization. **Luca di Mare:** Supervision, Software, Methodology, Formal analysis, Conceptualization. **Mauro Carnevale:** Writing – original draft, Supervision, Software, Resources, Project administration, Funding acquisition, Conceptualization.

#### Declaration of competing interest

The authors declare that they have no known competing financial interests or personal relationships that could have appeared to influence the work reported in this paper.

#### Acknowledgement

This work used the ARCHER2 UK National Supercomputing Service (<https://www.archer2.ac.uk>) [42]. This research did not receive any specific grant from funding agencies in the public, commercial, or not-for-profit sectors.

#### Data availability

Data will be made available on request.

#### References

- [1] Reynolds WC. On the potential and limitations of direct and large eddy simulations. In: Lumley JL, editor. *Whither turbulence? Turbulence at the crossroads*. New York: Springer-Verlag; 1990, p. 313–43. [http://dx.doi.org/10.1007/3-540-52535-1\\_52](http://dx.doi.org/10.1007/3-540-52535-1_52).
- [2] Vreman B, Geurts B, Kuerten H. Subgrid-modelling in LES of compressible flow. *Appl Sci Res* 1995;54(3):191–203. <http://dx.doi.org/10.1007/BF00849116>.
- [3] Sagaut P. Subgrid-scale modeling: Issues and approaches. In: *Implicit large eddy simulation: computing turbulent fluid dynamics*. Cambridge University Press; 2007, p. 61–93. <http://dx.doi.org/10.1017/CBO9780511618604.005>.
- [4] Piomelli U. *Large eddy simulation and related techniques*. 2022.
- [5] Grinstein FF, Margolin LG, Rider WJ. A rationale for implicit LES. In: *Implicit large eddy simulation: computing turbulent fluid dynamics*. Cambridge University Press; 2007, p. 39–58. <http://dx.doi.org/10.1017/CBO9780511618604.004>.

- [6] Boris JP. On large eddy simulation using subgrid turbulence models comment 1. In: Lumley JL, editor. *Whither turbulence? Turbulence at the crossroads*. Berlin, Heidelberg: Springer Berlin Heidelberg; 1990, p. 344–53. [http://dx.doi.org/10.1007/3-540-52535-1\\_53](http://dx.doi.org/10.1007/3-540-52535-1_53).
- [7] Colella P, Woodward PR. The piecewise parabolic method (PPM) for gas-dynamical simulations. *J Comput Phys* 1984;54(1):174–201. [http://dx.doi.org/10.1016/0021-9991\(84\)90143-8](http://dx.doi.org/10.1016/0021-9991(84)90143-8).
- [8] Harten A. High resolution schemes for hyperbolic conservation laws. *J Comput Phys* 1983;49(3):357–93. [http://dx.doi.org/10.1016/0021-9991\(83\)90136-5](http://dx.doi.org/10.1016/0021-9991(83)90136-5).
- [9] Yee H, Warming R, Harten A. Implicit total variation diminishing (TVD) schemes for steady-state calculations. *J Comput Phys* 1985;57(3):327–60. [http://dx.doi.org/10.1016/0021-9991\(85\)90183-4](http://dx.doi.org/10.1016/0021-9991(85)90183-4).
- [10] Hope-Collins J, di Mare L. Artificial diffusion for convective and acoustic low mach number flows I: Analysis of the modified equations, and application to Roe-type schemes. *J Comput Phys* 2023;475:111858. <http://dx.doi.org/10.1016/j.jcp.2022.111858>.
- [11] Li Z, Zhang Y, Chen H. A low dissipation numerical scheme for implicit large Eddy simulation. *Comput & Fluids* 2015;117:233–46. <http://dx.doi.org/10.1016/j.compfluid.2015.05.016>.
- [12] Uranga A, Persson P-O, Drela M, Peraire J. Implicit large Eddy simulation of transition to turbulence at low Reynolds numbers using a discontinuous Galerkin method. *Internat J Numer Methods Engrg* 2011;87(1–5):232–61. <http://dx.doi.org/10.1002/nme.3036>.
- [13] Ollivier-Gooch C, Ollivier-Gooch C. High-order ENO schemes for unstructured meshes based on least-squares reconstruction. In: 35th aerospace sciences meeting and exhibit. 1997, p. 1–14. <http://dx.doi.org/10.2514/6.1997-540>.
- [14] Rosafio N, Salvadori S, Misul DA. Implementation of a high-order spatial discretization into a finite volume solver: Applications to turbomachinery test cases using an eddy-viscosity turbulence closure. *Heliyon* 2024;10(16):e36478. <http://dx.doi.org/10.1016/j.heliyon.2024.e36478>.
- [15] Camarri S, Salvetti MV, Koobus B, Dervieux A. Large-eddy simulation of a bluff-body flow on unstructured grids. *Internat J Numer Methods Fluids* 2002;40(11):1431–60. <http://dx.doi.org/10.1002/flid.425>.
- [16] Amirante D, Hills NJ. Large-Eddy simulations of wall bounded turbulent flows using unstructured linear reconstruction techniques. *J Turbomach* 2015;137(5):051006. <http://dx.doi.org/10.1115/1.4028549>.
- [17] Barth T, Jespersen D. The design and application of upwind schemes on unstructured meshes. In: 27th aerospace sciences meeting. 1989, p. 1–13. <http://dx.doi.org/10.2514/6.1989-366>.
- [18] di Mare L, Kulkarni DY, Wang F, Romanov A, Ramar PR, Zachariadis ZI. Virtual gas turbines: Geometry and conceptual description. In: Volume 1: aircraft engine; ceramics; coal, biomass and alternative fuels; wind turbine technology. *Turbo expo: power for land, sea, and air*, 2011, p. 347–58. <http://dx.doi.org/10.1115/GT2011-46437>.
- [19] Hadade I, Wang F, Carnevale M, di Mare L. Some useful optimisations for unstructured computational fluid dynamics codes on multicore and manycore architectures. *Comput Phys Comm* 2019;235:305–23. <http://dx.doi.org/10.1016/j.cpc.2018.07.001>.
- [20] Wang F, Carnevale M, Lu G, di Mare L, Kulkarni D. Virtual gas turbine: Pre-processing and numerical simulations. In: Volume 1: aircraft engine; fans and blowers; marine. *Turbo expo: power for land, sea, and air*, 2016, V001T01A009. <http://dx.doi.org/10.1115/GT2016-56227>.
- [21] Carnevale M, Green JS, Di Mare L. Numerical studies into intake flow for fan forcing assessment. In: Volume 1A: aircraft engine; fans and blowers. *Turbo expo: power for land, sea, and air*, 2014, V01AT01A019. <http://dx.doi.org/10.1115/GT2014-25772>.
- [22] Carnevale M, Wang F, di Mare L. Low frequency distortion in civil aero-engine intake. *J Eng Gas Turbines Power* 2016;139(4):041203. <http://dx.doi.org/10.1115/1.4034600>.
- [23] Wang F, Carnevale M, di Mare L. Numerical study of deterministic fluxes in compressor passages. *J Turbomach* 2018;140(10):101005. <http://dx.doi.org/10.1115/1.4041450>.
- [24] Wang F, Carnevale M, di Mare L, Gallimore S. Simulation of multistage compressor at off-design conditions. *J Turbomach* 2017;140(2):021011. <http://dx.doi.org/10.1115/1.4038317>.
- [25] De Cosmo G, Scobie JA, Lock GD, Sangan CM, Carnevale M. Fluid dynamics of turbine rim seal structures: A physical interpretation using URANS. *J Eng Gas Turbines Power* 2022;145(3):031009. <http://dx.doi.org/10.1115/1.4055752>.
- [26] White JA, Nishikawa H, Baurle RA. Weighted least-squares cell-average gradient construction methods for the VULCAN-CFD second-order accurate unstructured grid cell-centered finite-volume solver. In: AIAA scitech 2019 forum. 2019, p. 1–28. <http://dx.doi.org/10.2514/6.2019-0127>.
- [27] Nishikawa H. On the loss and recovery of second-order accuracy with U-MUSCL. *J Comput Phys* 2020;417:109600. <http://dx.doi.org/10.1016/j.jcp.2020.109600>.
- [28] Wilcox DC. Formulation of the k-w turbulence model revisited. *AIAA J* 2008;46(11):2823–38. <http://dx.doi.org/10.2514/1.36541>.
- [29] Shih T-H, Liou WW, Shabbir A, Yang Z, Zhu J. A new k- $\epsilon$  eddy viscosity model for high reynolds number turbulent flows. *Comput Fluids* 1995;24(3):227–38. [http://dx.doi.org/10.1016/0045-7930\(94\)00032-T](http://dx.doi.org/10.1016/0045-7930(94)00032-T).
- [30] Blazek J. *Computational fluid dynamics: Principles and applications*, third ed.. Oxford: Butterworth-Heinemann; 2015. <http://dx.doi.org/10.1016/C2013-0-19038-1>.
- [31] Thornber B, Mosedale A, Drikakis D, Youngs D, Williams R. An improved reconstruction method for compressible flows with low mach number features. *J Comput Phys* 2008;227(10):4873–94. <http://dx.doi.org/10.1016/j.jcp.2008.01.036>.
- [32] Rieper F. A low-mach number fix for Roe's approximate Riemann solver. *J Comput Phys* 2011;230(13):5263–87. <http://dx.doi.org/10.1016/j.jcp.2011.03.025>.
- [33] Bui TT. A parallel, finite-volume algorithm for large-eddy simulation of turbulent flows. *Comput & Fluids* 2000;29(8):877–915. [http://dx.doi.org/10.1016/S0045-7930\(99\)00040-7](http://dx.doi.org/10.1016/S0045-7930(99)00040-7).
- [34] Boniface J-C. Rescaling of the Roe scheme in low Mach-number flow regions. *J Comput Phys* 2017;328:177–99. <http://dx.doi.org/10.1016/j.jcp.2016.10.011>.
- [35] Wang Z, Fidkowski K, Abgrall R, Bassi F, Caraeni D, Cary A, Deconinck H, Hartmann R, Hillewaert K, Huynh H, Kroll N, May G, Persson P-O, van Leer B, Visbal M. High-order CFD methods: current status and perspective. *Internat J Numer Methods Fluids* 2013;72(8):811–45. <http://dx.doi.org/10.1002/flid.3767>.
- [36] Taylor G. Statistical theory of turbulence. *Proc R Soc Lond Ser A, Math Phys Sci* 1935;151(873):421–44. <http://dx.doi.org/10.1098/rspa.1935.0158>.
- [37] Comte-Bellot G, Corrsin S. Simple Eulerian time correlation of full-and narrow-band velocity signals in grid-generated, 'isotropic' turbulence. *J Fluid Mech* 1971;48(2):273–337. <http://dx.doi.org/10.1017/S0022112071001599>.
- [38] Saad T, Cline D, Stoll R, Sutherland JC. Scalable tools for generating synthetic isotropic turbulence with arbitrary spectra. *AIAA J* 2017;55(1):327–31. <http://dx.doi.org/10.2514/1.J055230>.
- [39] McDermott RJ. *Toward one-dimensional turbulence subgrid closure for large-eddy simulation* (Ph.D. thesis), University of Utah; 2005, URL <https://ui.adsabs.harvard.edu/abs/2005PhDT.....160M>.
- [40] Pope SB. *Turbulent flows*. Cambridge University Press; 2000. <http://dx.doi.org/10.1017/CBO9780511840531>.
- [41] Banchetti J, Luchini P, Quadrio M. Turbulent drag reduction over curved walls. *J Fluid Mech* 2020;896:A10. <http://dx.doi.org/10.1017/jfm.2020.338>.
- [42] Beckett G, Beech-Brandt J, Leach K, Payne Z, Simpson A, Smith L, Turner A, Whiting A. *Archer2 service description*. Zenodo; 2024. <http://dx.doi.org/10.5281/zenodo.14507040>.